# Mode Coupling in Dynamic Atomic Force Microscopy

Abhilash Chandrashekar,[1,*] Pierpaolo Belardinelli,[2] Stefano Lenci,[2] Urs Staufer,[1] and Farbod Alijani[1,†]

[1] *Precision and Microsystems Engineering, TU Delft, Delft, Netherlands*
[2] *DICEA, Polytechnic University of Marche, Ancona, Italy*

(Received 2 October 2020; revised 17 December 2020; accepted 13 January 2021; published 4 February 2021)

Increasing the signal-to-noise ratio in dynamic atomic force microscopy plays a key role in nanomechanical mapping of materials with atomic resolution. In this work, we develop an experimental procedure for increasing the sensitivity of higher harmonics of an atomic-force-microscope cantilever without modifying the cantilever geometry but instead by utilizing dynamical mode coupling between its flexural modes of vibration. We perform experiments on different cantilevers and samples and observe that via nonlinear resonance frequency tuning we can obtain a frequency range where strong modal interactions lead to 7-fold and 16-fold increases in the sensitivity of the 6th and 17th harmonics while reducing sample indentation. We derive a numerical model that captures the observed physics and confirms that nonlinear mode coupling is the reason for the increase of the amplitude of higher harmonics during tip-sample interactions.

DOI: 10.1103/PhysRevApplied.15.024013

## I. INTRODUCTION

Dynamic atomic force microscopy (AFM) has emerged as a powerful tool for nanoscale imaging of matter in many technical and scientific application areas [1]. In dynamic AFM, an oscillating microcantilever tip interacts intermittently with the sample while being driven close to or at a resonance frequency. Dynamic AFM is routinely used to characterize the topography of samples with nanometer or even atomic resolution. Irrespective of the outstanding capabilities offered by this AFM mode, the understanding of nanoscale processes and quantification of material properties using AFM are still far from being well established. One reason curbing this is that in conventional dynamic AFM experiments a single drive frequency is used to scan the sample and the feedback system maintains either the amplitude or the phase of oscillations constant. As a result, the number of observable channels that are required to quantify the mechanical properties of the sample are not sufficient. To overcome this limitation, multifrequency-AFM techniques are being adopted [2]. These methods use mainly higher harmonics of the cantilever deflection signal [3,4] or the output signals of two or three resonant modes [5,6] to obtain complementary information of the interacting sample. Other modes of multifrequency AFM are also available that use torsional harmonics [7] or intermodulation products [8] to probe sample properties.

To date, many studies have incorporated the aforementioned multifrequency-AFM techniques to map nanomechanical properties of samples, ranging from polymeric substances [9,10] to biological substances [11,12]. However, only a handful of these studies have looked into the possibilities for enhancing the sensitivity of the higher-order spectral components [7,13–16]. Among them, most have exploited a phenomenon known as internal resonance [17]. This condition occurs when the ratio between two or more resonance frequencies of the cantilever is a rational number, and results in strong coupling between the interacting modes of vibration [18]. The significance of intermodal coupling arises from its correlation with the effective spring constant of the resonant modes that can be tuned by modifying the geometry of the cantilever [7,14], by creating notches or holes [15], or by adding a concentrated mass at specific locations on the cantilever [16].

Here, in contrast to previous studies, we propose a technique to increase the signal-to-noise ratio (SNR) of higher harmonics and higher-order flexural modes of an atomic-force-microscope cantilever without the need to modify its geometry. By sweeping the drive frequency in the spectral neighborhood of a resonance, we find a frequency range where strong interactions between the first three flexural modes of the cantilever significantly increase the amplitude of higher harmonics. Using this technique, we are able to increase the amplitude of the 6th and 17th harmonics by 7-fold and 16-fold, respectively. Driving the cantilever in this frequency range also results in decreased sample indentation due to the phase

---

[*] a.chandrashekar@tudelft.nl
[†] f.alijani@tudelft.nl

synchronization of the eigenmodes. These phenomena are showcased at drive amplitudes comparable to the set-point ratios used in conventional scanning operation, thereby highlighting the utility of the technique in dynamic AFM. To understand the physics behind our observations, we develop a theoretical model comprising multiple degrees of freedom and nonsmooth nonlinear interactions between the tip and the sample. Our simulations qualitatively conform with the observed physics, and confirm that mode coupling is responsible for the increase in the SNR of higher harmonics. Our study also reveals the use of real-time temporal data for identifying dynamical coupling in AFM applications. Because of its simplicity and ease of use, the proposed technique has the potential to be used in a variety of multifrequency-AFM techniques.

## II. EXPERIMENTAL RESULTS

Our experiments are performed using a commercial atomic force microscope (JPK Nanowizard) and two separate data-acquisition electronic devices—namely, a multi-lock-in amplifier from Intermodulation Products and a field-programmable gated array (FPGA) from National Instruments—to collect and analyze the cantilever deflection data. We use a commercially available rectangular silicon cantilever (NCLR, NanoWorld AG) and a flat silicon sample to perform the experiments. For each experiment, the spring constant of the cantilever ($k = 22.68$ N/m), its resonance frequency ($f_0 = 164.52$ kHz), and its quality factor ($Q = 428$) are determined by the thermal-calibration method [19]. A schematic of the setup is shown in Fig. 1(a).

To obtain the nonlinear resonance response of the atomic-fore-microscope cantilever while it is interacting with the sample, we implement a procedure where a standard force-distance curve is first used to statically approach the sample surface with a small set point of 2 nm. Next, the end condition of the force-distance curve is preserved to hold the cantilever at the precise fixed distance $\eta^*$ of 100 nm from the sample surface. The latter operation is feasible with use of the feedback loop on the $z$ piezo scanner of the atomic force microscope, which stays active for a specific period of time. While the static position ($\eta^*$) is maintained, the drive frequency ($f_d$) of the dither piezo is swept around the resonance frequency from 163 to 170 kHz ($f_0 = 164.52$ kHz). The resulting change in vibrational amplitude is recorded with the multi-lock-in amplifier and the FPGA simultaneously. Additionally, during the entire sweep duration a specific excitation $y(t)$ is applied such that the reduction in vibrational amplitude due to tip-sample interaction is maintained at 84%. This reduction is comparable with that of the amplitude set-point ratios used during normal scanning operation in dynamic AFM (see Fig. S1.1 in Supplemental Material S1 [20]). The outcome of this procedure is shown in Fig. 1(b). It can be seen that when the deflection amplitude is increased, the resonance curve first slightly bends to the left (spring softening) [21] and as the tip further approaches the sample, the curve bends toward the right side of the resonance (spring hardening). The presence of nonlinear attractive and repulsive forces between the tip and the sample lies at the root of our observation [22].

In Fig. 1(b) we also observe that the nonlinear-resonance curve obtained by use of the lock-in amplifier (pink curve)

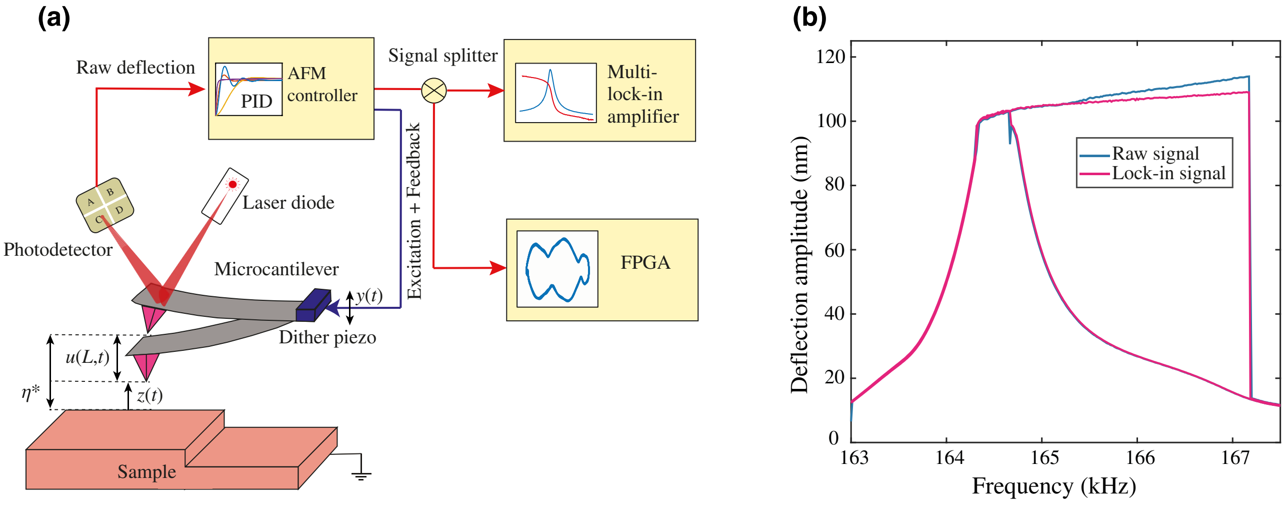

FIG. 1. The experimental setup and the acquired experimental nonlinear dynamic response. The response is obtained with a commercial rectangular cantilever (NCLR, NanoWorld AG) on a silicon sample with an excitation amplitude of 0.013 V. (a) The setup using two different data-acquisition electronic devices—namely, a multi-lock-in amplifier and a FPGA device. The schematic details the initial static cantilever configuration $\eta^*$ and the dynamic configuration with the cantilever vibrating about the elastostatic equilibrium $u$ at the free end $L$ of the cantilever. (b) The blue and pink curves indicate the nonlinear dynamic response obtained with the raw deflection signal and the lock-in signal. The forward and reverse sweeps are combined into one curve.

is different from the one obtained by analyzing the raw deflection signal using the FPGA (blue curve). We observe a mismatch in the amplitudes of the two signals that increases at higher $f_d$. The observed discrepancy hints at the presence of higher-order spectral components that are essentially eliminated when the lock-in amplifier is used. This is because the lock-in amplifier allows detection of a single frequency component when sweeping $f_d$ around resonance and effectively approximates the cantilever dynamics as a single-degree-of-freedom system. However, the FPGA stores the real-time deflection signal and thus can efficiently capture modal interactions that may exist around the resonance.

To further investigate the cantilever's nonlinear dynamic response, we obtain the maximum and minimum of the deflection in an oscillatory cycle using the FPGA [see Fig. 2(a)]. The cantilever deflection signal reaches a maximum far from the sample, whereas the minimum shows that the tip is interacting with the sample. This segregation reveals a broken symmetry in the response due to the nonsmooth nature of the contact between the tip and the sample when $f_d$ is detuned from $f_0$. To study the physical origin of this symmetry-breaking response, we trace the phase-space trajectories of the cantilever in real time when moving from $f_d = 164.5$ kHz to $f_d = 167$ kHz [see Figs. 2(b) and 2(c)]. The phase-space trajectories are highly sensitive to the presence of higher-order modes and can be used to identify modal interactions [22]. In Fig. 2(b) we observe simple harmonic oscillations of the cantilever close to the free-air resonance ($f_d = 164.5$ kHz); however, at large detuning ($f_d \geq 166.4$ kHz), the phase space warps, and ripples appear on the periphery of the trajectory [Fig. 2(c)]. To understand the origin of this phase-space distortion, we perform fast Fourier transform of the temporal data [see Figs. 2(d) and 2(e)], and observe that the frequency content of the signal at $f_d = 164.5$ kHz involves only $f_0$ and a few of its higher harmonics. But, when applying fast Fourier transform on the time signal taken at $f_d = 167$ kHz, we find an additional resonance peak appears at $f_2 = 1020$ kHz [see Fig. 2(e)], suggesting the activation of the second eigenmode of the cantilever. In essence, this shows that the phase-space distortions are a direct result of activation of higher-order vibrational modes and that the presence of higher harmonics has a trivial effect on these trajectories (see Fig. 6 in Appendix A for details).

To elaborate on our observation, we note that for the cantilever used in the experiments, the frequency ratio $f_2/f_0 \approx 6.2$ is close to the factor 6. Therefore, by tuning the nonlinear resonance frequency (by sweeping $f_d$), we can reach a 6:1 internal resonance in the frequency range $f_d \in [165, 166]$ kHz, where the contribution of the second mode becomes apparent. The resulting mode coupling enhances the SNR of specific harmonics that are close to the interacting eigenmode. In particular, we observe a

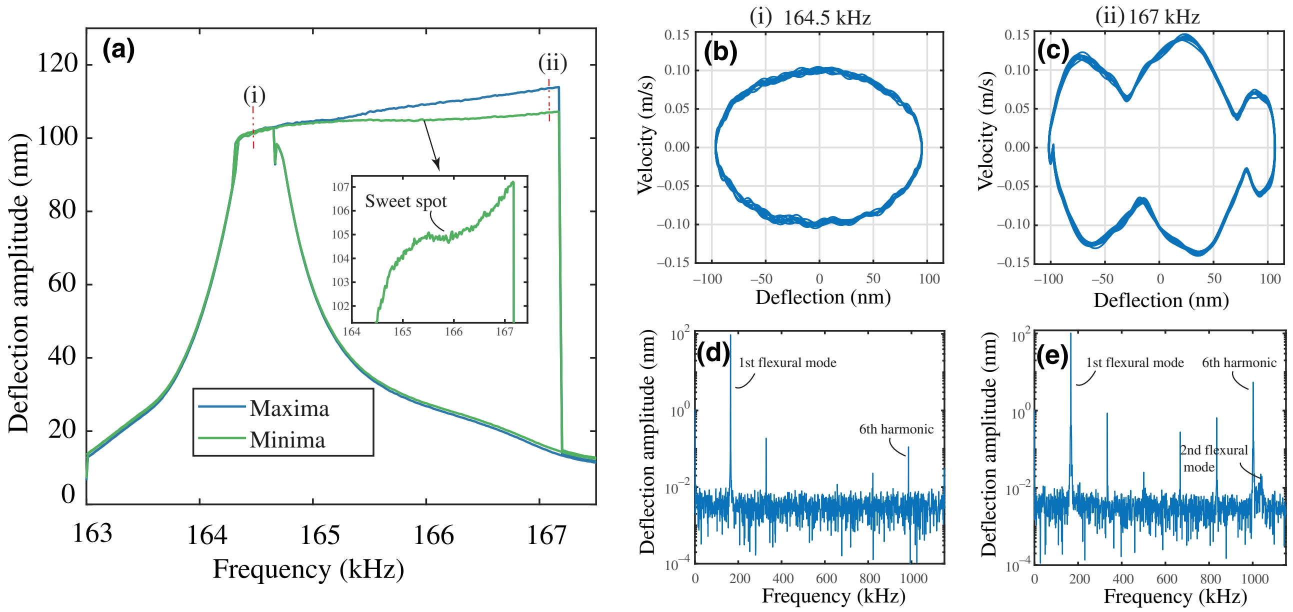

FIG. 2. Experimental nonlinear dynamic response, phase-space trajectories, and the associated frequency spectra obtained from the raw deflection signal of the cantilever. (a) Experimental frequency-response curve; the blue and green curves represent the maximum and minimum positions of the tip, respectively. The forward and reverse sweeps are combined into one curve. The inset highlights the gradual curving of the nonlinear dynamic response in a specific range of the drive frequency. The sweet-spot frequency range is highlighted by dashed lines. (b),(c) Phase-space trajectories at drive frequencies of 164.5 and 167 kHz showing the influence of the second eigenmode in the cantilever oscillations. (d),(e) Frequency spectra of the raw deflection signal at 164.5 and 167 kHz showing the presence of higher harmonics and the second eigenmode.

sevenfold increase in the SNR of the sixth harmonic compared with its amplitude near the free-air resonance [see Figs. 2(d) and 2(e)].

This modal interaction is not only characterized by an increase in the strength of harmonics but is also accompanied by a reduced sample indentation when compared with normal scanning operations with similar amplitude set-point ratios at $f_d = f_0$. As we sweep $f_d$ around the resonance, we observe a decrease in the minimum amplitudes in the 165 kHz $< f_d <$ 166 kHz frequency range, which is associated with a decrease in the sample indentation. Such properties make the frequency range over which mode coupling occurs an ideal excitation range for the mapping of nanomechanical properties. Therefore, we label this region as the "sweet spot." This lower sample indentation is highlighted in the inset in Fig. 2(a), and can be formally described as a gradual curving of the nonlinear-dynamic-response curve in its deflection minima forming a convex shape. It may be intuitively thought that the increased coupling should increase the interaction force and, as a consequence, increase the sample indentation. However, in the sweet spot, the phases of the interacting modes synchronize in such a way that there is a reduced sample indentation (see Fig. 8 in Appendix C). This dynamic feature is similar to what has been reported in dynamically tuned trapezoidal cantilevers [14].

To investigate the repeatability of the observed phenomena, we perform an additional set of experiments using a TAP190Al-G rectangular cantilever on a highly-oriented-pyrolytic-graphite sample, a TAP300Al-G rectangular cantilever on a nanocrystalline-diamond island and a TAP150AL-G rectangular cantilever on a polystyrene island. We find that the "sweet spot" is not a unique feature that belongs to a particular sample-cantilever configuration (for details see Sec. B in Supplemental Material S1 [20]). These interesting observations highlight the role of higher eigenmodes and mode coupling in AFM applications.

## III. MODELING AND SIMULATIONS

To underpin the physics behind our experimental observations and to further understand the nature of the mode coupling, we develop a theoretical model based on a nonsmooth two-degree-of-freedom system. The derivation of the model can be found in Appendix B. The model uses the long-range nonlinear van der Waals (vdW) and Derjaguin-Muller-Toporov (DMT) contact forces to describe the tip-sample interactions $F_{ts}(z)$ as follows [23,24]:

$$F_{ts}(z) = \begin{cases} F_{\mathrm{vdW}} = -\dfrac{HR}{6z^2} \quad \text{for} \quad z > a_0, \\ F_{\mathrm{DMT}} = -\dfrac{HR}{6{a_0}^2} + \dfrac{4}{3}E^*\sqrt{R}\,(a_0 - z)^{3/2} \\ \qquad \text{for} \quad z \leq a_0, \end{cases} \tag{1}$$

where $H$ stands for the Hamaker constant, $R$ the tip radius, $a_0$ the intermolecular distance, and $E^*$ the effective Young's modulus. The tip-surface interaction is purely attractive ($F_{\mathrm{vdW}}$) when the separation distance $z$ is larger than the intermolecular distance $a_0$. If $z$ is smaller than $a_0$, the interaction is governed by contact mechanics ($F_{\mathrm{DMT}}$). This nonsmoothness in the interaction force mediates an energy channel between different modes of the cantilever and acts as the root cause of our observation.

To obtain the equations of motion, we model the atomic-force-microscope cantilever as a continuous dynamical system using the Euler-Bernoulli beam theory. We discretize the model by projecting the cantilever deflection onto its linear eigenmodes (computed near free-air resonance) and use the Galerkin approach to obtain a system of ordinary differential equations as follows [22]:

$$\ddot{\tilde{q}}_i + D_i\left(\bar{z}\right)\dot{\tilde{q}}_i + K_i\tilde{q}_i = -C_i - F_{ts,i}\left(\bar{z}\right) + B_i\bar{\Omega}^2\bar{y}\sin\bar{\Omega}\tau. \tag{2}$$

The cantilever deflection, split across the generalized coordinates $\bar{q}_i$ $(i = 1, 2, \ldots N$, with $N$ being the number of generalized coordinates), is written in Eq. (2) for a reference system attached to the cantilever [see Fig. 1(a)]. The coupling between the generalized coordinates occurs through the relation $\bar{z} = 1 - \sum_{i=1}^{n}\tilde{q}_i - \bar{y}\sin\bar{\Omega}\tau$. In addition, Eq. (2) is made dimensionless with respect to the equilibrium gap width ($\eta^*$) and the fundamental frequency of the cantilever ($\omega_0 = 2\pi f_0$) in the absence of the tip-sample interaction. The amplitude of the dither piezo is given by $\bar{y}$, and the dotted quantities represent derivatives with respect to the rescaled time $\tau$ ($\tau = \omega_0 t$). Additionally, modal damping $D_i(\bar{z})$ has been explicitly added to Eq. (2). In particular, we consider a piecewise model [23] that accounts for the dissipation mechanism when the tip is in air ($\tilde{D}_i^{\mathrm{att}}$) or when it is in contact with the sample ($\tilde{D}_i^{\mathrm{rep}}$). Finally, the coefficients $K_i$, $C_i$, and $B_i$ represent the modal stiffness, static deflection, and mode-participation factor, respectively. The final discretized equation is then simulated using a pseudo-arc-length-continuation technique to fit the experimental data [25,26].

The simulations performed using the two-mode vdW-DMT model qualitatively describe our experimental observations. In Fig. 3(a) the blue and green nonlinear-dynamic-response curves represent the maximum and minimum deflection of the cantilever, similar to what is observed in experiments. In Fig. 3(a), the gradual curving of the minimum response (green curve) occurs when the simulation parameters of the coupled oscillator system are tuned to produce a 6:1 internal resonance condition, confirming the presence of this unconventional internal resonance at a detuning of a few kilohertz (for details see Sec. C in Supplemental Material S1 [20]). Adding to this, the theoretical nonlinear-dynamic-response curves highlight the

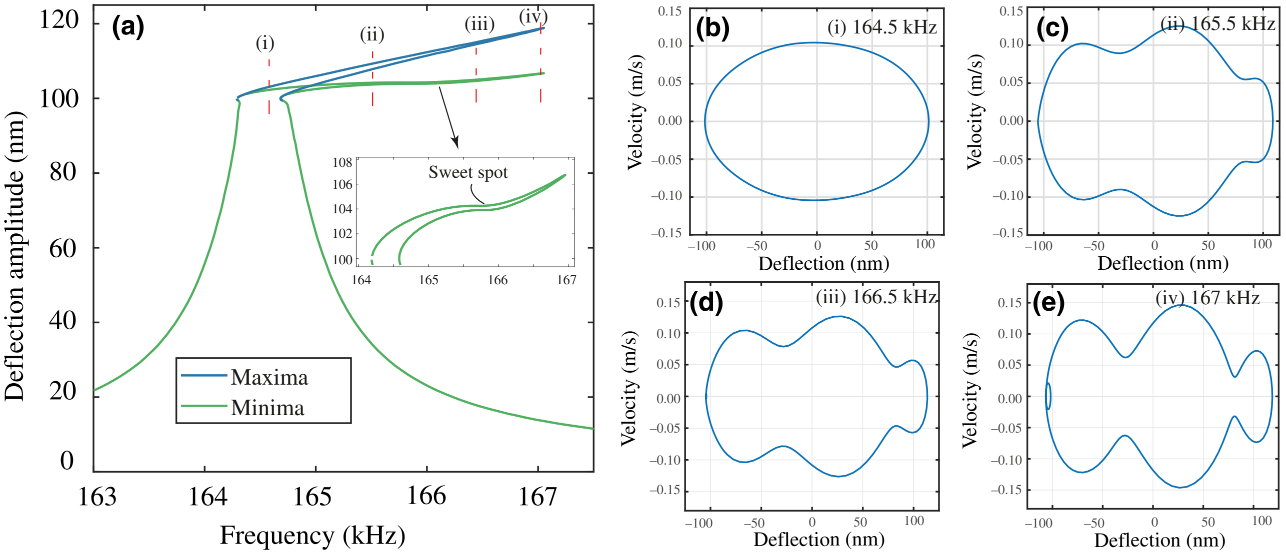

FIG. 3. Simulated nonlinear dynamic response and phase-space trajectories obtained with the two-mode model. (a) Numerical frequency response curve; the blue and green curves represent the maximum and minimum positions of the tip, respectively. The forward and reverse sweeps are combined into one curve. The nonlinear dynamic response is simulated considering 6:1 internal resonance between the first two flexural modes. The inset highlights the gradual curving of the nonlinear dynamic response in a specific range of the drive frequency. The sweet-spot frequency range is highlighted by dashed lines. (b)–(e) Phase space trajectories at drive frequencies of 164.5, 165.5, 166.5, and 167 kHz, respectively.

influence of the higher-order modes in the distortion of the phase-space trajectory. Similarly to the experimental results, the periodic orbit exhibits simple harmonic motion close to free-air resonance [Fig. 3(b)], which becomes distorted by detuning $f_d$ to higher frequencies. The distortion gradually increases in depth, in accordance with the contribution given by the second mode of vibration [Figs. 3(c)–3(e)].

Although the two-mode model accurately predicts the dominance of the second mode at large detunings and explains the physics behind the curving of the nonlinear dynamic response in the sweet spot, it masks the effect of any further couplings that may exist among higher modes of vibration. In particular, as depicted in Fig. 4, at $f_d =$ 165.5 kHz we observe an increase in the number of ripples on the periphery of the phase space (blue curve). This additional distortion of the phase space is accompanied by a 16 fold increase in the amplitude of the 17th harmonic, which is located close to the third flexural mode of the cantilever ($f_3 \approx 17.5 f_0$). To prove our hypothesis about the influence of the third flexural mode, we low-pass filter the experimental data up to the 16th harmonic and observe that the resulting phase space (orange curve) closely matches that of the simulated trajectory obtained with the two-mode-approximation model shown in Fig. 3(c). Although including an additional mode in the numerical model (with consequent increase of the complexity in the simulations) could capture completely the dynamics observed in experiments, it would not add physical insights for the observations reported in this paper.

Finally, as an extensive view of the various stages of the influence of higher-order modes as $f_d$ is detuned from $f_0$, we report in Fig. 5 the variation of the 6th and 17th harmonics as a function of $f_d$. At first, when $f_d$ is close to $f_0$, the amplitude of the harmonics generated due to tip-sample forces is relatively low and comparable with the

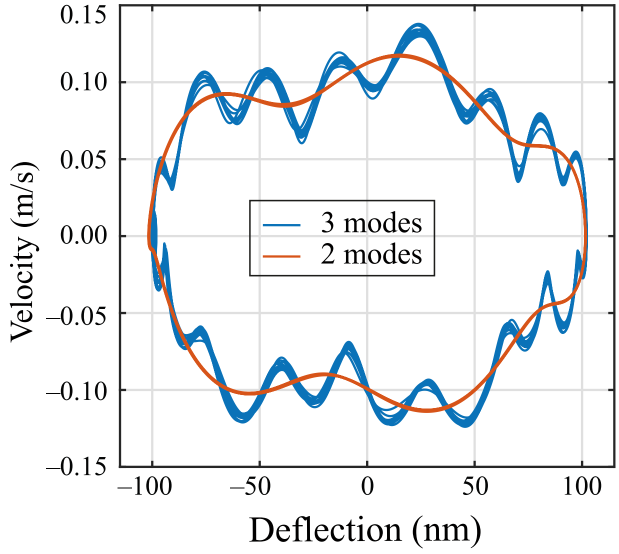

FIG. 4. Phase-space trajectories obtained from experimental deflection at $f_d = 165.5$ kHz. The experimental deflection signal is low-pass filtered with different cutoff frequencies to identify the contribution from the second flexural mode (orange curve) and the third flexural mode (blue curve).

strength of the signals observed during normal tapping-mode scanning operation. In the low-frequency range (green region in Fig. 5) the entire cantilever dynamics can be well approximated as a single-degree-of-freedom system. With increased detuning, when $f_d$ lies in the sweet spot (orange region), there is sharp increase in the contribution of the second and third eigenmodes in the cantilever motion and the dynamics is governed by the three flexural modes of the cantilever. In this region the amplitudes of the 6th and 17th harmonics increase by 7-fold and 16-fold, respectively, as a consequence of an enhanced mode coupling both with the second eigenmode and with the third eigenmode. On further detuning, we observe a continuous increase of SNR of the sixth harmonic but at the expense of increased sample indentation. At the same time, the large resonance-frequency tuning causes the amplitude of the 17th harmonic to drop gradually, until the contribution of the third mode completely disappears. In the violet region in Fig. 5, the dynamics is fully governed by the first mode and the second mode only. Additionally, by increasing the amplitude of the excitation, the sweet spot widens by a few kilohertz, while the physics remains unaltered. However, this increase in the sweet-spot range comes at the expense of a larger set-point ratio (for details see Fig. S1.5 in Supplemental Material S1 [20]).

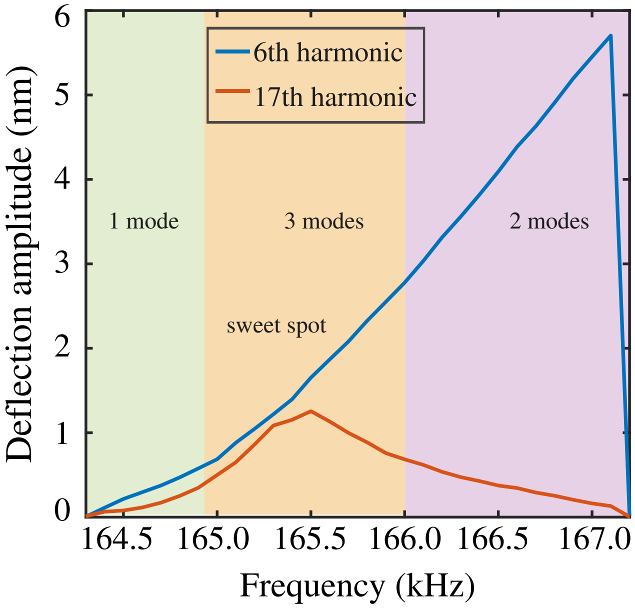

FIG. 5. Variation of the amplitudes of the 6th and 17th harmonics as a function of the drive frequency $f_d$. The amplitudes of the 6th and 17th harmonics increase in a specific frequency range highlighted by the orange section due to intermodal coupling. Thereafter, only the amplitude of the sixth harmonic increases due to increased tip-sample interaction and dominance of the second mode of vibration.

Currently, the method provides a significant increase in the SNR of higher harmonics for single-point measurements and could be implemented in techniques that extract the nanomechanical properties of samples at several predetermined pixels. However, to integrate the technique with conventional scanning operation there are a few limitations that still need to be addressed. In particular, as a first step, the algorithm routine used to capture the raw deflection signal and tune the nonlinear resonance frequency has to be integrated into the atomic force microscope's controller in order to handle the data processing at imaging speeds. Such integration also helps tackle the issue of choosing the right drive frequency within the sweet spot for samples comprising multiple materials. Secondly, since the sweet spot is driven beyond the bifurcation point into a bistable region, a thorough study has to be performed to understand the influence of noise and feedback settings on the robustness of the sweet spot during imaging [27,28]. In this regard, our technique can be incorporated together with the latest feedback architectures, such as modulated time delay control [29], that have already been successfully used to control cantilever oscillations in the bistable regime and reduce perturbation-induced jumps during the scanning operation. Finally, it is important to consider the influence of the geometric and modal characteristics of the cantilever used for performing the measurements. The technique reported in this paper has been showcased with standard rectangular cantilevers and is applicable to cantilevers with the second and the third bending modes close to $6f_0$ and $17f_0$, respectively.

## IV. CONCLUSION

In summary, we propose a technique to actively tune the nonlinear resonance frequency of atomic-force-microscope cantilevers to achieve a high SNR of harmonics at low sample indentation compared with conventional dynamic AFM operations. We discuss the influence of higher-order modes on the phase-space trajectories of the cantilever as a function of the detuned frequency and highlight the presence of a sweet spot in a specific frequency range around the resonance where there is a significant increase in the amplitude of higher harmonics due to strong modal interactions. We use a two-mode nonlinear nonsmooth model to qualitatively describe our experiments and explain the observed physics. The model reinforces the idea of mode coupling as the phenomenon behind the increase in the amplitude of higher harmonics and the lower sample indentation. Finally, given the ease of use and utility, we anticipate that this experimental technique can be used together with various multifrequency-AFM techniques to study nanomechanical properties of organic and inorganic samples without the need for specialized cantilevers. Our technique can also be easily used in multifrequency scanning operations to obtain images of the higher harmonics with increased sensitivity, which is an essential requirement in dynamic AFM applications.

## ACKNOWLEDGMENTS

This work is part of the research program “A NICE TIP TAP” with Grant No. 15450, which is financed by the Netherlands Organisation for Scientific Research (NWO). The authors also acknowledge fruitful discussions with Dr. Oriel Shoshani about internal resonance, Dr. Gerard Verbiest regarding the experiments, Dr. Daniel Forchheimer for FPGA coding, and Dr. André F. Sartori for sample preparation.

## APPENDIX A: INFLUENCE OF HARMONICS ON PHASE-SPACE TRAJECTORIES

In this section, we study the influence of harmonics and higher-order modes on the phase-space trajectories and present additional results to corroborate our findings. In particular, we focus on the warping of the phase-space trajectories and its insensitivity to higher harmonics. Figure 6 shows the experimental phase-space trajectories and the associated frequency spectra at several distinct excitation frequencies. The data are extracted from the nonlinear-frequency-response curve [Fig. 2(a)]. The time data are digitally low-pass filtered at different stages with different cutoff frequencies to understand the influence of higher-order spectral components. At first, we choose a frequency point close to the resonance at $f_d = 164.4$ kHz and obtain the phase-space trajectories and the corresponding frequency spectra as shown in Figs. 6(a) and 6(b). The data are digitally low-pass filtered with a cutoff frequency of 3.5 MHz. In Fig. 6(a), the frequency spectrum clearly shows the presence of several higher harmonics, and in particular the 6th and 17th harmonics are of special interest since they are closer to the second and third flexural modes of the cantilever and thus show more contrast in AFM imaging operations. From these figures, even when the higher harmonics are present in the cantilever deflection, the phase-space trajectories remain approximately circular and show no signs of warping [see Fig. 6(b)].

In the next step of the analysis, we choose the frequency point $f_d = 165.5$ kHz reported in Fig. 4 but low-pass filter the time data with two different cutoff frequencies—namely 1.1 MHz (up to the 7th harmonic) [Fig. 6(c),(d)] and 2.65 MHz (up to the 16th harmonic)

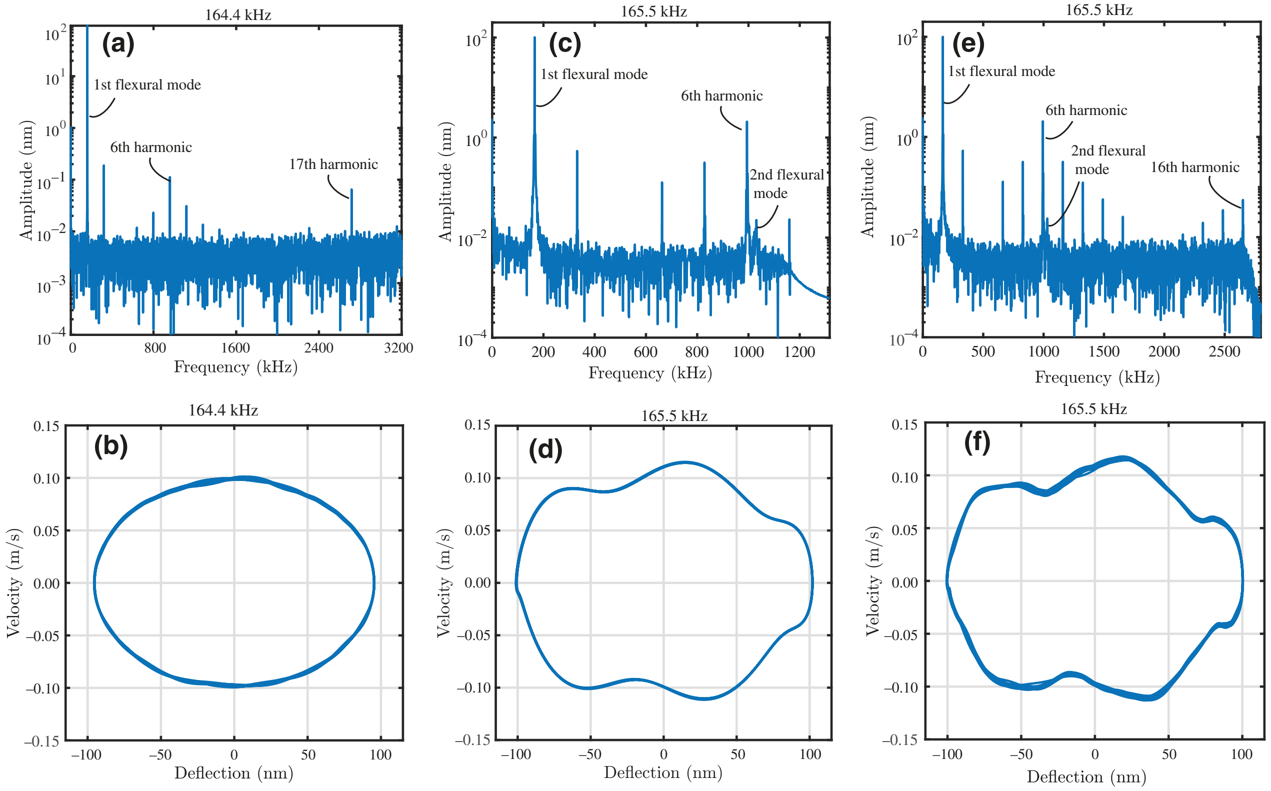

FIG. 6. Influence of harmonics and higher-order eigenmodes on phase-space trajectories. (a),(b) Discrete frequency spectra and the associated phase-space trajectories at $f_d = 164.4$ kHz. (c),(d) Discrete frequency spectra and the associated phase space trajectories at $f_d = 165.5$ kHz. The time data are low-pass filtered to include the first seven harmonics of the cantilever. (e),(f) Discrete frequency spectra and the associated phase space trajectories at $f_d = 165.5$ kHz. The time data are low-pass filtered to include the first 16 harmonics of the cantilever.

[Fig. 6(e) and 6(f)]. From the frequency spectrum in Fig. 6(c), we see that by including spectral components only until the second mode, we see a gradual warping of the phase space with characteristic ripples appearing on its periphery [see Fig. 6(d)]. Furthermore, by including the spectral components up to the 16th harmonic [see Fig. 6(e)], we see that the shape of the phase-space trajectory is unaltered [see Fig. 6(f)]. However, if the time data at this particular frequency point were not low-pass filtered, then the shape would resembled the phase-space trajectory shown in Fig. 4. This analysis shows the insensitivity of the phase-space trajectories to higher harmonics and further highlights the utility of phase-space orbits as tools for probing the presence of higher-order eigenmodes and modal interactions in dynamic AFM applications.

## APPENDIX B: THEORETICAL MODEL

Here we obtain the dynamical equation for the atomic-force-microscope cantilever initially resting in a static equilibrium at a distance $\eta^*$ from the sample (see Fig. 7). The mathematical framework to develop the continuous model for the atomic-force-microscope cantilever is within the assumptions of Euler-Bernoulli beam theory. The atomic-force-microscope cantilever has length $L$, mass density $\rho$, Young's modulus $E$, area moment of inertia $I$, and cross-section area $A$. The beam is clamped at $x = 0$ and free at $x = L$. The cantilever deflection is expressed in a noninertial reference frame attached to the base, and the cantilever is excited with harmonic motion $y(t) = Y \sin \Omega t$ via a dither piezo, where $Y$ and $\Omega$ are the amplitude and frequency of excitation, respectively. The static deflection due to tip-sample forces at $\eta^*$ is given by $w^*(x)$ [see Fig. 7(a)]. Finally, the instantaneous tip-sample distance $z(t) = \eta^* - u(L,t) - y(t)$, where $u(x,t)$ is the dynamic deflection of the cantilever as shown in Fig. 7(b). The vibrations about the elastostatic equilibrium are governed by the equation [23]

$$\rho A\ddot{u}(x,t) + EI[u''''(x,t) + w^{*''''}(x)] \\ = F_{ts}(z(t))\delta(x-L) + \rho A\Omega^2 Y \sin \Omega t. \tag{B1}$$

We discretize Eq. (B1) by projecting it onto linear mode shapes $\phi_i(x)$ computed around the cantilever static configuration. For this, we approximate the response as

$$u(x,t) = \sum_{i=1}^{n} \phi_i(x) q_i(t), \tag{B2}$$

with $q_i(t)$ being the generalized time-dependent coordinate for the $i$th mode of vibration. We then substitute Eq. (B2) in Eq. (B1) and by using the Galerkin procedure, we take the inner products with the same shape functions used in the discretization. The final discretized dimensionless set of nonlinear ordinary differential equations is as follows:

$$\ddot{\tilde{q}}_i + D_i(\bar{z})\dot{\tilde{q}}_i + K_i\tilde{q}_i = -C_i - F_{ts,i}(\bar{z}) + B_i\bar{\Omega}^2\bar{y}\sin\bar{\Omega}\tau, \tag{B3}$$

where $\bar{z}$ is the dimensionless tip-sample separation distance given by

$$\bar{z} = 1 - \sum_{i=1}^{n} \tilde{q}_i - \bar{y}\sin\bar{\Omega}\tau. \tag{B4}$$

Substituting Eq. (B4) in the equation for the tip-sample interaction force [Eq. (1)], we obtain

$$F_{ts,i}(\bar{z}) = \begin{cases} C_i/\bar{z}^2, & \text{for} \quad \bar{z} > \bar{a}_0, \\ C_i/\bar{a}_0^2 + G_i(\bar{a}_0 - \bar{z})^{3/2}, & \text{for} \quad \bar{z} \le \bar{a}_0, \end{cases} \tag{B5}$$

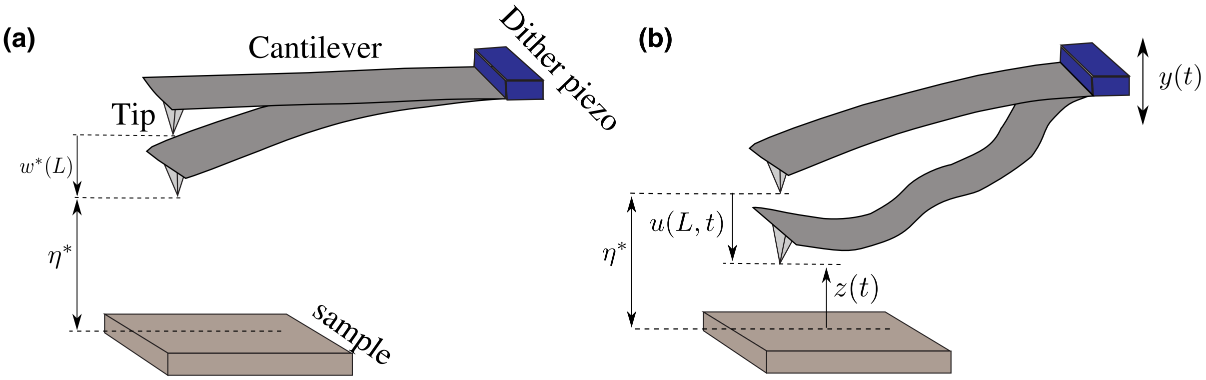

FIG. 7. (a) Initially statically deflected configuration of the atomic force microscope. (b) Dynamic configuration of the atomic force microscope with the cantilever vibrating about its elastostatic equilibrium.

where the coefficients arising in Eqs. (B3) and (B5) are defined as

$$K_i = \frac{{\omega_i}^2}{{\omega_0}^2}, \quad C_i = -\frac{HR{\phi_i}^2(L)}{6\rho A{\eta^*}^3{\omega_0}^2\int_0^L {\phi_i}^2(x)\,dx},$$

$$B_i = \frac{\phi_i(L)\int_0^L \phi_i(x)\,dx}{\int_0^L {\phi_i}^2(x)\,dx}, \quad G_i = \frac{4E^*\sqrt{R\eta^*}{\phi_i}^2(L)}{3\rho A{\omega_0}^2\int_0^L {\phi_i}^2(x)\,dx}. \tag{B6}$$

In the formulation presented the generalized coordinates $\tilde{q}_i$ are normalized with respect to the value of the mode shape at the free end of the cantilever [$\tilde{q}_i = \phi_i(L)\,q_i$]. The overdot in Eq. (B3) means differentiation with respect to dimensionless time—namely, $\tau = \omega_0 t$, where $\omega_0$ is the fundamental frequency of the cantilever. The amplitude and frequency of the excitation, $Y$ and $\Omega$, are related to their dimensionless counterparts through $\bar{y} = Y/\eta^*$ and $\bar{\Omega} = \Omega/\omega_0$, respectively. Finally, $\bar{a}_0 = a_0/\eta^*$ is the dimensionless conjugate of the intermolecular distance $a_0$. Note that the modal damping $D_i(\bar{z})$ is considered in Eq. (B3). Similarly to Ref. [23], we consider a piecewise model that accounts for the dissipation mechanisms while the tip is in air ($\tilde{D}_i^{\text{att}}$) or in contact with the sample ($\tilde{D}_i^{\text{rep}}$):

$$D_i(\bar{z}) = \begin{cases} {D_i}^{\text{att}} = \dfrac{\tilde{D}_i^{att}}{\omega_0\rho A\int_0^L {\phi_i}^2(x)\,dx}, & \text{for} \quad \bar{z} > \bar{a}_0, \\ {D_i}^{\text{rep}} = \dfrac{\tilde{D}_i^{rep}}{\omega_0\rho A\int_0^L {\phi_i}^2(x)\,dx}, & \text{for} \quad \bar{z} \le \bar{a}_0. \end{cases} \tag{B7}$$

In our simulations we restrict ourselves to a two-degree-of-freedom model, which means we limit Eq. (B3) to $i = 2$. In this case the coupled set of nonlinear differential equations becomes

$$\begin{aligned} &\ddot{\tilde{q}}_1 + D_1^{\text{att}}\dot{\tilde{q}}_1 + K_1\tilde{q}_1 = -C_1 - \frac{C_1}{\left(1 - \tilde{q}_1 - \tilde{q}_2 - \bar{y}\sin\bar{\Omega}\tau\right)^2} \\ &\quad + B_1\bar{\Omega}^2\bar{y}\sin\bar{\Omega}\tau, \\ &\ddot{\tilde{q}}_2 + D_2^{\text{att}}\dot{\tilde{q}}_2 + K_2\tilde{q}_2 = -C_2 - \frac{C_2}{\left(1 - \tilde{q}_1 - \tilde{q}_2 - \bar{y}\sin\bar{\Omega}\tau\right)^2} \\ &\quad + B_2\bar{\Omega}^2\bar{y}\sin\bar{\Omega}\tau, \end{aligned} \tag{B8}$$

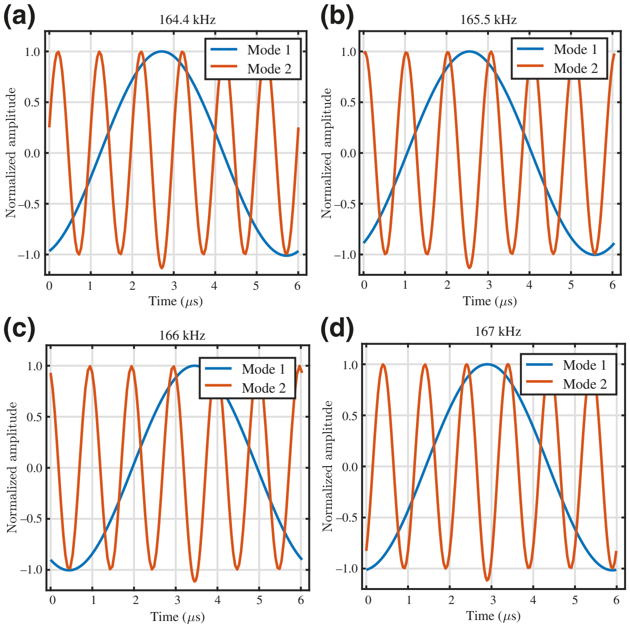

FIG. 8. Simulations depicting auto phase synchronization between the first (blue) and second (orange) flexural modes in the sweet spot. To aid with the visualization, the amplitudes of the time signals are normalized with respect to their corresponding maximum value in a given time period. (a) At resonance, the oscillations of the first and second flexural modes start with a phase difference of 90°. (b),(c) Phase difference between the two eigenmodes in the sweet spot at 165.5 and 166 kHz, respectively. (d) Phase difference between the two modes out of the sweet spot at 167 kHz.

$$\begin{aligned} &\ddot{\tilde{q}}_1 + D_1^{\text{rep}}\dot{\tilde{q}}_1 + K_1\tilde{q}_1 = -C_1 - C_1/\bar{a}_0^2 \\ &\quad -G_1\left[\bar{a}_0 - \left(1 - \tilde{q}_1 - \tilde{q}_2 - \bar{y}\sin\bar{\Omega}\tau\right)\right]^{3/2} \\ &\quad +B_1\bar{\Omega}^2\bar{y}\sin\bar{\Omega}\tau, \\ &\ddot{\tilde{q}}_2 + D_2^{\text{rep}}\dot{\tilde{q}}_2 + K_2\tilde{q}_2 = -C_2 - C_2/\bar{a}_0^2 \\ &\quad -G_2\left[\bar{a}_0 - \left(1 - \tilde{q}_1 - \tilde{q}_2 - \bar{y}\sin\bar{\Omega}\tau\right)\right]^{3/2} \\ &\quad +B_2\bar{\Omega}^2\bar{y}\sin\bar{\Omega}\tau, \end{aligned} \tag{B9}$$

where Eq. (B8) and (B9) are integrated with the conditions $\left(1 - \tilde{q}_1 - \tilde{q}_2 - \bar{y}\sin\bar{\Omega}\tau\right) \le \bar{a}_0$ and $(1 - \tilde{q}_1 - \tilde{q}_2 - \bar{y}\sin\bar{\Omega}\tau\big) > \bar{a}_0$, respectively.

The simulation parameters used in Eqs. (B8) and (B9) to obtain the results presented in Fig. 3 are provided in Supplemental Material S2 [20].

## APPENDIX C: PHASE SYNCHRONIZATION AT INTERNAL RESONANCE

We report a reduction in sample indentation in Fig. 2(a) when $f_d$ is detuned to coincide with the sweet spot. Here we use the simulations from our two-mode vdW-DMT model described in Eq. (B9) and show that the phase synchronization between the eigenmodes is responsible for the aforementioned reduction in sample indentation. Figure 8 shows the time signals of the first (blue) and second (orange) flexural modes extracted from the same simulations reported in Fig. 3. The signals are extracted at different excitation frequencies from the nonlinear-frequency-response curve to track the variation of the phase difference between the two modes. At resonance $f_d = f_0$ [see Fig. 8(a)] the phase difference between the two modes is approximately 90°. However, when $f_d$ is detuned to enter the sweet spot [see Figs. 8(b) and 8(c)], the phase difference changes drastically such that the two modes interact almost in out-of-phase motion. The phase difference between the two modes changes from 152.11° to 163.38° as $f_d$ is swept from 165.5 to 166 kHz. This out-of-phase motion between the two eigenmodes results in destructive interference, causing a reduced sample indentation. Finally, when $f_d$ is out of the sweet-spot range, the phase difference gradually shrinks to 32.4° at 167 kHz [see Fig. 8(d)]. This reduction in phase difference causes the two modes to interfere constructively and therefore results in larger indentation at higher excitation frequencies.

All the data in this paper are available from the authors on request.

[1] Y. F. Dufrêne, T. Ando, R. Garcia, D. Alsteens, D. Martinez-Martin, A. Engel, C. Gerber, and D. J. Müller, Imaging modes of atomic force microscopy for application in molecular and cell biology, Nat. Nanotechnol. **12**, 295 (2017).

[2] R. Garcia, and E. T. Herruzo, The emergence of multifrequency force microscopy, Nat. Nanotechnol. **7**, 217 (2012).

[3] R. Hillenbrand, M. Stark, and R. Guckenberger, Higher-harmonics generation in tapping-mode atomic-force microscopy: Insights into the tip–sample interaction, Appl. Phys. Lett. **76**, 3478 (2000).

[4] M. Stark, R. W. Stark, W. M. Heckl, and R. Guckenberger, Spectroscopy of the anharmonic cantilever oscillations in tapping-mode atomic-force microscopy, Appl. Phys. Lett. **77**, 3293 (2000).

[5] E. T. Herruzo, A. P. Perrino, and R. Garcia, Fast nanomechanical spectroscopy of soft matter, Nat. Commun. **5**, 1 (2014).

[6] D. Martinez-Martin, E. T. Herruzo, C. Dietz, J. Gomez-Herrero, and R. Garcia, Noninvasive protein structural flexibility mapping by bimodal dynamic force microscopy, Phys. Rev. Lett. **106**, 198101 (2011).

[7] O. Sahin, Time-varying tip-sample force measurements and steady-state dynamics in tapping-mode atomic force microscopy, Phys. Rev. B **77**, 115405 (2008).

[8] D. Platz, E. A. Tholén, D. Pesen, and D. B. Haviland, Intermodulation atomic force microscopy, Appl. Phys. Lett. **92**, 153106 (2008).

[9] R. Garcia, and R. Proksch, Nanomechanical mapping of soft matter by bimodal force microscopy, Eur. Polym. J. **49**, 1897 (2013).

[10] P.-A. Thorén, R. Borgani, D. Forchheimer, I. Dobryden, P. M. Claesson, H. G. Kassa, P. Leclère, Y. Wang, H. M. Jaeger, and D. B. Haviland, Modeling and measuring viscoelasticity with dynamic atomic force microscopy, Phys. Rev. Appl. **10**, 024017 (2018).

[11] A. Raman, S. Trigueros, A. Cartagena, A. P. Stevenson, M. Susilo, E. Nauman, and S. A. Contera, Mapping nanomechanical properties of live cells using multi-harmonic atomic force microscopy, Nat. Nanotechnol. **6**, 809 (2011).

[12] M. Dong, S. Husale, and O. Sahin, Determination of protein structural flexibility by microsecond force spectroscopy, Nat. Nanotechnol. **4**, 514 (2009).

[13] R. Potekin, S. Dharmasena, D. M. McFarland, L. A. Bergman, A. F. Vakakis, and H. Cho, Cantilever dynamics in higher-harmonic atomic force microscopy for enhanced material characterization, Int. J. Solids Struct. **110–111**, 332 (2017).

[14] A. Keyvani, H. Sadeghian, M. S. Tamer, J. F. L. Goosen, and F. van Keulen, Minimizing tip-sample forces and enhancing sensitivity in atomic force microscopy with dynamically compliant cantilevers, J. Appl. Phys. **121**, 244505 (2017).

[15] O. Sahin, G. Yaralioglu, R. Grow, S. F. Zappe, A. Atalar, C. Quate, and O. Solgaard, High-resolution imaging of elastic properties using harmonic cantilevers, Sens. Actuators A: Phys. **114**, 183 (2004).

[16] H. Li, Y. Chen, and L. Dai, Concentrated-mass cantilever enhances multiple harmonics in tapping-mode atomic force microscopy, Appl. Phys. Lett. **92**, 151903 (2008).

[17] A. H. Nayfeh, and D. T. Mook, *Nonlinear oscillations* (John Wiley & Sons, 2008).

[18] Ata Keskekler, Oriel Shoshani, Martin Lee, Herre S. J. van der Zant, Peter G. Steeneken, and Farbod Alijani, Enhancing nonlinear damping by parametric-direct internal resonance, arXiv:2006.09364v3 (2020).

[19] J. E. Sader, J. W. M. Chon, and P. Mulvaney, Calibration of rectangular atomic force microscope cantilevers, Rev. Sci. Instrum. **70**, 3967 (1999).

[20] See Supplemental Material at http://link.aps.org/supplemental/10.1103/PhysRevApplied.15.024013 for additional details regarding the calculation of the set-point ratio, additional experimental data sets, numerical simulations depicting the importance of internal resonance, discussion of the influence of the excitation amplitude on the sweet spot, and information regarding the simulation parameters used in the paper.

[21] E. Rull Trinidad, T. Gribnau, P. Belardinelli, U. Staufer, and F. Alijani, Nonlinear dynamics for estimating the tip radius in atomic force microscopy, Appl. Phys. Lett. **111**, 123105 (2017).

[22] A. Chandrashekar, P. Belardinelli, U. Staufer, and F. Alijani, Robustness of attractors in tapping mode atomic force microscopy, Nonlinear Dyn. **97**, 1137 (2019).

[23] S. I. Lee, S. W. Howell, A. Raman, and R. Reifenberger, Nonlinear dynamic perspectives on dynamic force microscopy, Ultramicroscopy **97**, 185 (2003).

[24] R. García, and A. San Paulo, Attractive and repulsive tip-sample interaction regimes in tapping-mode atomic force microscopy, Phys. Rev. B **60**, 4961 (1999).

[25] H. Dankowicz, and F. Schilder, *Recipes for Continuation, Computational Science and Engineering* (Society for Industrial and Applied Mathematics, 2013).

[26] B. Krauskopf, H. M. Osinga, and J. Galan-Vioque, *Numerical Continuation Methods for Dynamical Systems: Path Following and Boundary Value Problems* (Springer Netherlands, 2007).

[27] Andrew N. Round, and Mervyn J. Miles, Exploring the consequences of attractive and repulsive interaction regimes in tapping mode atomic force microscopy of DNA, Nanotechnology 15 (2004).

[28] Robert W. Stark, Bistability, higher harmonics, and chaos in AFM, Mater. Today **13**, 24 (2010).

[29] Ilham Kirrou, and Mohamed Belhaq, Control of bistability in non-contact mode atomic force microscopy using modulated time delay, Nonlinear Dyn. **81**, 607 (2015).